

# Designing Coupling Behaviors Using Compliant Shape Optimization

Nurcan Gecer Ulu<sup>a</sup>, Stelian Coros<sup>b</sup>, Levent Burak Kara<sup>a,\*</sup>

<sup>a</sup>Carnegie Mellon University, 5000 Forbes Avenue, Pittsburgh, PA 15213 USA

<sup>b</sup>ETH Zurich, Universitaetstrasse 6, Zurich, 8092 Switzerland



Figure 1: We introduce a method for designing coupling behaviors between an arbitrary compliant structure and an arbitrary rigid object. Resulting structures exhibit the desired coupling behavior such as ease of engagement/disengagement and grip.

## Abstract

A wide set of assembly blocks such as attachments, connectors, joints, and supports rely on the principle of passively coupling two objects using structural compliance. However, only a limited variety of configurations are prevalent in daily use (*e.g.*, snap fits) due to the challenge of extending the appropriate mechanical behavior to arbitrary object pairs. In this work, we present a method for computationally designing the mechanical coupling behavior between a rigid object and a compliant enclosure based on high-level specifications such as the ease of engagement and disengagement. At the heart of our approach is the use of deformation profiles as the means to describe and optimize physical coupling characteristics. In particular, we introduce a method that maps the shape parameters of the compliant object onto sequentially observed coupling descriptors such as the grip, insertion and removal forces that develop as the rigid object is engaged. Using this formulation, we present a method for optimizing the rest shape of the compliant object to produce the desired coupling behavior. We demonstrate our approach through a variety of designs and validate it with 3D printed physical prototypes.

## 1. Introduction

Mechanical coupling, defined as attaching two objects to one another, is a fundamental notion that underpins the realization of all types of connectors, joints, fixtures and attachments, which enable the creation of complex assemblies and mechanisms [1]. In daily use, a large class of couplings are intended to be *readily separable* with as few parts as possible as a way to facilitate temporary affixing, quick assembly and maintenance, and general ease of use. To this end, passive coupling of objects through structural compliance is a widely used method involving minimal number of parts and mechanical complexity, as part engagement is primarily enabled by elastic body deformations over coupling rigid objects. For designing monolithic compliant structures, topology optimization is a widely used approach that allows a tuning of force-displacement characteristics at prescribed end states [2, 3], or to achieve structures that satisfy strength or compliance

requirements under specified load configurations [4].

However, only a limited variety of configurations are prevalent in daily use (*e.g.*, snap fits) due to the challenge of extending the appropriate mechanical behavior to arbitrary object pairs. In particular, the compliant structures and their rigid counterparts are typically tailored such that either there exists known and permanent contact points that do not change during coupling [5], or the contact points involving the maximally deformed state can be known *a priori* [6]. Realizing these limitations, Koyama et al. [7] in an inspiring work present a data-driven approach for designing compliant attachments using parameterized basic geometries such as cylinders and rectangular prisms. However, the analysis does not extend to arbitrary free-form objects, necessitating rigid, multi-part solutions for such instances.

In this work, we present a physics-based method for designing the mechanical coupling behavior between a rigid and a compliant object such that the engagement and dis-

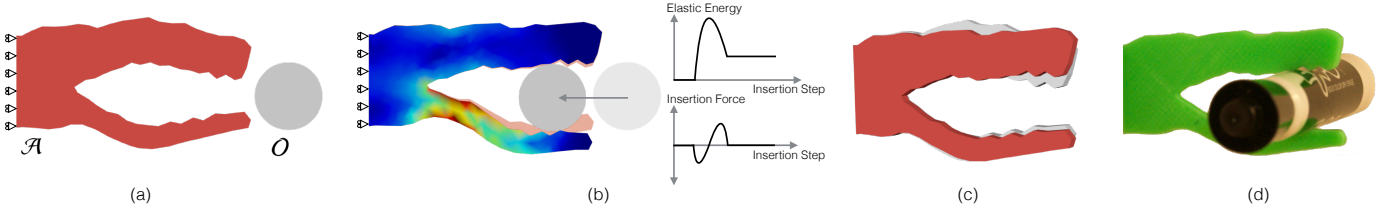


Figure 2: Given a compliant structure  $\mathcal{A}$  and a rigid object  $\mathcal{O}$  (a), our algorithm optimizes the rest shape of  $\mathcal{A}$  based on the deformation behavior obtained through insertion simulations (b). The resulting structure (c) exhibits the desired compliant behavior when coupled with  $\mathcal{O}$  (d). Grey silhouette in (c) is the original unmodified shape.

engagement forces during the process of coupling, as well as the grip forces that lock the object pair together can all be customized by optimizing the shape of the compliant object (Figure 1). Given an arbitrary rigid and compliant object, we use deformation profiles as a means to describe and optimize physical coupling. We introduce a method that maps the compliant object’s shape parameters onto sequentially observed coupling descriptors such as the grip, insertion and removal forces that develop when the compliant object engages the rigid object. Using this formulation, we present a method for optimizing the rest shape of the compliant object to produce the desired coupling behavior.

A distinguishing feature of our approach is that it allows coupling behaviors to be designed for part interactions that may not be known *a priori*. In particular, our approach does not rely on the knowledge of known contact points or deformed states, thereby extending prior work on compliant attachments to scenarios involving arbitrary object pairs.

Our main contributions are

- The use of deformation profiles to describe and optimize mechanical behavior.
- A physics based shape optimization method for compliant coupling behavior design involving two-part interactions.
- A practical insertion simulation based on collision elimination for computing deformation profiles.

## 2. Related Work

Fundamentally, our approach involves mechanical behavior control through shape optimization. Below, we review the works that are foundational to our work.

*Deformation Behavior Control.* Deformation control through shape and structure optimization has been addressed in various ways including (1) Material distribution optimization [8, 9, 10], (2) Multi-material distributions [11], (3) Wireframe thickness optimization [12], and (4) Nonlinear material design through prescribed stress-strain curves [13]. Xu et al. [14] introduce model reduction to design heterogeneous deformable materials to achieve prescribed displacements and forces. Chen et al. [6] explore

rest shape optimization to account for the deformations due to prescribed forces to obtain desired deformed states.

We extend these works to scenarios involving a coupling process with part contacts between a compliant and a rigid object rather than relying on forces known *a priori*. We formulate a broader problem where the compliant object acquires its final (steady) state through a progression of contacts where neither the location of the contact, nor the resulting contact forces can be known in advance. Additionally, it is not possible to prescribe the final deformed configuration in advance, as the contact forces deforming the object cannot be known explicitly *a priori*. Finally, each new hypothesis for the compliant object during its design likely produces new contact configurations. This necessitates shape design and contact analysis to be performed conjointly.

*Computational Design for Fabrication.* There exists a large body of work for structure design to enable prescribed functional objectives such as kinematic goals [15, 16, 17], strength improvements [18, 19, 20, 21], or other physical qualities of interest [22, 23, 24]. Closely related to our work [7] create automatic connectors between object pairs involving parameterized primitive geometries such as cylinders and rectangular prisms using a data-driven approach informed by a battery of physical experiments, or use partitioned rigid connectors to accommodate free-form objects. Our work extends their work by formulating compliant mechanical coupling design as a conjoint shape optimization and physics-based contact simulation. This allows our method to transform arbitrary free-form objects into pairs that can be made attachable to one another.

*Compliant Mechanisms.* Compliant mechanisms exploit flexible and continuous joint structures [25]. Typically, compliant mechanisms are structurally optimized for input/output displacement or force transfer ratios [2, 3], for matching the displacement path of a compliant mechanism for an input actuation [26], or for enabling gripping behavior through known input force points [27, 28, 29, 30, 31]. Our compliant structures are not externally activated through prescribed contact points. Instead, deformations are generated through part interactions that are unknown *a priori*.

Bruns et al. [30] present a designer guided topology optimization method for generating a snap-fit mechanism to



Figure 3: Example compliant couplings as part of our daily lives. Image courtesy of TRS Prosthetics, Expo, Chicco, ScribbleJ@Thingiverse.

mount onto walled openings. However, contacts are deterministic as they follow imposed boundaries such as continuous sliding across a line. Lawry et al. [32] present a topology optimization method that produces a snap fit pair starting from objects with perfectly matching boundaries (*i.e.*, one object is a complement of the other). The aim is to optimize harmonic separation forces without considering grip. Optimization of connectors for simple pin geometries has been shown in [33, 34]. Our approach builds on these ideas to make arbitrary geometries attachable to one another rather than fine-tuning existing snap fit configurations. With our formulation, engagement and disengagement forces as well as grip tightness can be designed in a decoupled way, thereby enabling the creation of couplings that require weak engagement forces but result in tight grips. Moreover, our work extends the above works in 2D to 3D.

*Contact Simulation.* Our approach seeks to optimize the compliant object so as to produce the desired deformation behavior in the form of deformation profiles. The deformation, however, depends exclusively on the interaction between the current shape of the compliant object and the rigid object, thus necessitates a heavy use of contact simulations throughout the shape optimization process. Kloosterman [35] provides a detailed review of the large body of research in contact simulations. Voxmap Point Shell [36] models the environment as a map of voxels for penetration calculations and computes virtual penalty forces to eliminate penetrations. This method works for rigid object contacts but it is also extended to deformable objects in [37]. Kaufman et al. [38] presents a method that can model the frictional contact between deformable objects. Complex contact scenarios in dynamic simulations are studied in [39]. Continuous penalty force approach is presented in [40]. Based primarily on these works, we formulate our insertion simulation as a friction-free penetration elimination problem using distance fields.

### 3. Fundamentals and Overview

Given a compliant structure  $\mathcal{A}$  and a rigid object  $\mathcal{O}$  to be inserted, we optimize the rest shape of  $\mathcal{A}$  (Figure 2). We use deformation profiles to understand and characterize

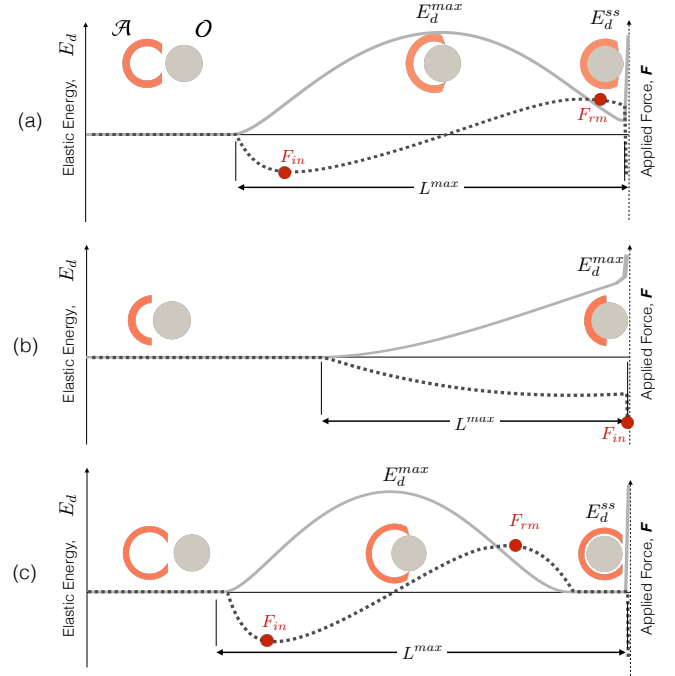


Figure 4: Deformation profiles for 3 different attachment categories (a-c). Relative positions of the compliant structure and the inserted object corresponding to initial, maximum  $E_d^{max}$ , and steady state  $E_d^{ss}$  energies are shown. Solid and dashed curves represent the elastic energy and applied force, respectively.

the coupling between  $\mathcal{A}$  and  $\mathcal{O}$  for the current hypothesis of  $\mathcal{A}$ .

#### 3.1. Deformation Profiles

Figure 3 shows example compliant couplings ubiquitous in consumer facing products. In all such couplings, the fundamental considerations are (i) how easy it is to engage and disengage the objects, and (ii) how tightly the objects are locked together in the fully inserted states (as depicted in Figure 3), with the obvious constraint that the compliant object should never break during its deformations.

As shown Figure 4, we use deformation profiles to capture both the elastic energy stored in the compliant object (solid line) as well as the resistive force it applies to the rigid object (dashed line) as a function of insertion distance. Qualitatively, a distinct steady state minimum in the elastic energy  $E_d^{ss}$  that is attained after passing through a maximum energy state  $E_d^{max}$  signals the presence of a valid coupling where no external force is necessary to keep the objects coupled (Figure 4(a),(c)). Furthermore, a non-zero  $E_d^{ss}$  implies a grip force locking the objects together (Figure 4(a)), while a zero  $E_d^{ss}$  implies a loose couple (Figure 4(c)). On the other hand, if a dip in the elastic energy is not present, this signals an engagement that would simply dissolve when the externally applied insertion forces are removed, *i.e.*,  $\mathcal{A}$  pushes out  $\mathcal{O}$  (Figure 4(b)).

### 3.2. Assumptions

We assume  $\mathcal{O}$  is rigid (does not deform), the engagement and disengagement are quasi-static, and the interactions are frictionless. As a result, all interaction forces develop exclusively due to the energy stored in  $\mathcal{A}$ . We discuss the impact of friction in the results section. We assume the mass center of  $\mathcal{O}$  cannot be pushed beyond  $\mathcal{A}$ 's farthest point (leftmost side of  $\mathcal{A}$  in Figure 4), hence capping the maximum theoretical deformation  $\mathcal{A}$  can undergo. This results in a maximum insertion length  $L^{max}$ . Users may provide insertion lengths that are shorter than this theoretical maximum.

### 3.3. Determining $E_d^{ss}$

We perform insertion simulations until  $L^{max}$ . Backtracking from the final state, we identify  $E_d^{ss}$  as the first local minimum in the elastic energy profile.

### 3.4. Force Characterization

*Insertion and Removal Forces.* With the assumption of quasi-static coupling, the insertion force is equivalent to the resistive force applied by  $\mathcal{A}$  to  $\mathcal{O}$ , and can be computed as the sum of forces at the fixed boundary nodes of  $\mathcal{A}$ . In Figure 4, we consider forces that resist the insertion of  $\mathcal{A}$  to be negative for notational convenience<sup>1</sup>. When disengaging the couple, the traversal is reversed. As a result, from the user's perspective, the negative forces (*e.g.*, the maximum negative) quantify the difficulty one experiences during insertion, while the positive forces quantify the difficulty during removal.

*Grip Forces.* Insertion and removal forces are different than the grip force that one usually attributes to how strongly the two objects are interlocked at  $E_d^{ss}$ . We define grip forces as a function of *all* the forces that  $\mathcal{O}$  experiences due to its contact with  $\mathcal{A}$  at  $E_d^{ss}$  (Section 5.2). In effect, the grip force characterizes the degree of squeeze  $\mathcal{A}$  imparts on  $\mathcal{O}$ .

## 4. Insertion Simulation

We represent the compliant attachment  $\mathcal{A}$  using a triangle mesh or a tetrahedral mesh  $\mathcal{M}$  in 2D and 3D cases. At each insertion step,  $\mathcal{O}$  is displaced by a prescribed step  $h_{in}$  and the corresponding deformed state of  $\mathcal{A}$  is computed.  $\mathcal{A}$  deforms to attain a minimum energy state while all penetrations into  $\mathcal{O}$  are precluded:

$$\begin{aligned} & \underset{x}{\text{minimize}} \quad E_d(x, X) \\ & \text{subject to} \quad \psi(x_j) < 0, \end{aligned} \quad (1)$$

where  $x$  and  $X$  denote the deformed and rest states of  $\mathcal{A}$ , as column vectors with concatenated vertex positions.  $E_d(x)$  and  $\psi(x_j)$  are elastic energy and penetration functions, respectively.  $\psi(x_j)$  is computed per vertex,  $x_j$ , denoting the position vector of a single vertex.

<sup>1</sup>Hence positive forces imply  $\mathcal{A}$  drawing in  $\mathcal{O}$ .

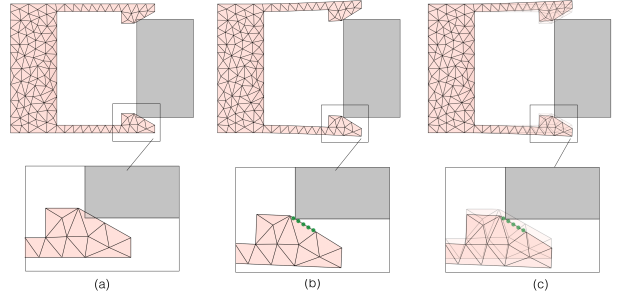


Figure 5: Effect of refinement. All vertices of  $\mathcal{A}$  are out of  $\mathcal{O}$  and the collision is not detected (a). With refinement, we interpolate new points on the colliding edges and check for collisions (b). Solutions with and without refinement are overlaid in (c).

### 4.1. Finite Element Model

We find the elastic energy of  $\mathcal{A}$  at the deformed state using finite element analysis. We use the rotation invariant Neo-Hookean material model to accommodate large deformations. While applicable to higher order element types, we use linear shape functions for simplicity. Using the Neo-Hookean material model and linear shape functions, the elastic energy is:

$$E_d(x) = V \left[ \frac{\mu}{2} (\|F\|_F^2 - \kappa_d) - \mu \log(\det(F)) + \frac{\lambda}{2} \log^2(\det(F)) \right], \quad (2)$$

where  $\mu$  and  $\lambda$  are Lamé parameters describing the material dependent stress and strain relationship.  $V$  and  $\kappa_d$  are volume and dimension constants which is 2 for 2D triangular elements and 3 for 3D tetrahedral elements.  $F = F(x, X)$  denotes the deformation gradient (*i.e.*  $F = dx/dX$ ) as a function of the current state,  $x$ , and the rest state,  $X$ , of  $\mathcal{A}$ . Further details can be found in [41].

The gradient of  $E_d(x, X)$  is computed using the first Piola-Kirchhoff stress tensor. We compute the reaction forces at the nodes of  $\mathcal{A}$  using the gradient as  $f = -\partial E_d(x, X)/\partial x$ . This way, we can compute the insertion forces from the reaction forces based on static equilibrium conditions.

We use the von Mises failure criterion to determine if  $\mathcal{A}$  fails ( $\sigma_{vm} < \sigma_{yield}$ ). We compute  $\sigma_{vm}$  from the Cauchy stress,  $\sigma_{cauchy}$ , by utilizing the already computed first Piola-Kirchhoff stress tensor,  $P$  with the following relation

$$\sigma_{cauchy} = (\det(F))^{-1} P F^T. \quad (3)$$

### 4.2. Avoiding Penetration

In order to expel the penetrating vertices of  $\mathcal{A}$  out of  $\mathcal{O}$ , we compute the shortest distance between all vertices of  $\mathcal{A}$  and  $\mathcal{O}$ . This way, we quantify how much  $\mathcal{A}$  has penetrated into  $\mathcal{O}$ . For this, we use the implicit moving least squares method (IMLS) to define a signed distance field on  $\mathcal{O}$ . This field is algebraically differentiable, thereby making

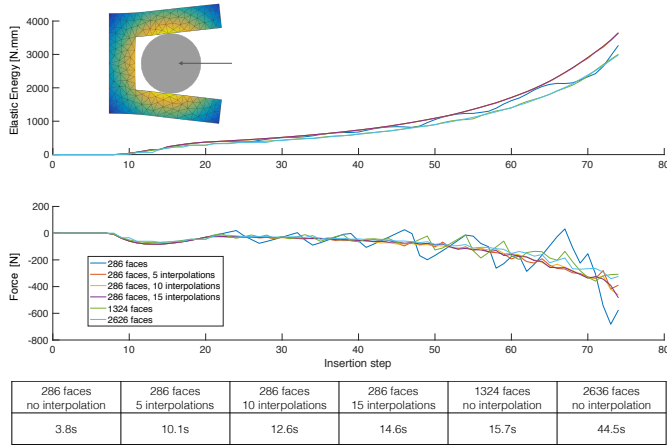


Figure 6: The effect of refinement, where smooth insertion forces are expected. The color on the attachment corresponds to the signed distance field of the circle. Note that refinement results in smoother force curves as well as requiring less computation compared to higher mesh resolutions.

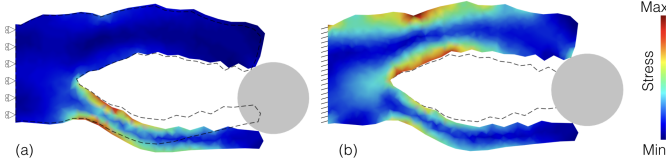


Figure 7: Effect of boundary conditions on asymmetrical attachments. The alligator is fixed on the left side. When only the insertion axis is fixed and the object is left free along the vertical axis, the results are more realistic stressing the thinner lower jaw (a). When all axes are fixed, the object pushes the thick upper jaw requiring larger insertion forces and causing higher energy states.

it suitable for optimization. Using Kolluri’s [42] implicit surface representation, our penetration function becomes

$$\psi(x_j) = -\frac{\sum_i n_i^T(x_j - v_i)\phi_i(x_j)}{\sum_i \phi_i(x_j)}, \quad (4)$$

where  $\phi_i(x_j) = e^{-\|x_j - v_i\|^2/\sigma^2}$  denotes the Gaussian kernel.  $x_j$  is the position vector of a vertex on  $\mathcal{A}$ ,  $v_i$  and  $n_i$  are the position and normal vectors of the  $i^{th}$  vertex on  $\mathcal{O}$ .  $\sigma$  is set empirically per  $\mathcal{O}$ .

#### 4.3. Finding Deformed States

The deformation of a compliant attachments is governed by Eq. (1), which is nonlinear in both the objective function and the constraints. At each insertion step, we employ Sequential Quadratic Programming (SQP) [43] to solve it. We use MOSEK [44] to solve arising sub quadratic problems.

*Refinement.* When  $\mathcal{A}$  is represented with a coarse mesh, collision checks involving only the vertices of  $\mathcal{A}$  may not be sufficient to prevent penetration (Figure 5). Moreover, these penetrations may result in oscillatory force profiles with poor accuracy as shown in Figure 6. As a remedy, we use the refinement described in Algorithm 1, where we

---

#### Algorithm 1: Energy minimization with refinement

---

```

Solve (1) with the vertices of  $\mathcal{A}$ ;
for each edge on the boundary of  $\mathcal{A}$  do
    if edge is in contact region then
        if edge is in collision with  $\mathcal{O}$  then
            | add the edge into the contact edge list,  $C_L$ ;
        end
    end
if  $C_L$  not empty then
    for each edge in  $C_L$  do
        | interpolate new points and add to constraint
        | list  $v_c$ ;
    end
    set initial conditions as the result of initial
    optimization;
    solve (1) with added constraints,  $v_c$ ;
end

```

---

check for collisions across the edges of  $\mathcal{A}$  close to the contact regions and sample the new vertices across those edges if intersections are found. The newly sampled vertices are added as additional penetration constraints. The same approach extends to 3D by sampling across the faces of  $\mathcal{A}$ . To determine the edges/faces to refine, we use the distance field already computed during the initial optimization step. We also use the IMLS surface field to check for collisions. Figure 6 illustrates the effect of refinement for various mesh and interpolation settings. In our examples, we use 10 interpolation points.

Oscillatory or non-smooth contact forces that arise due to discrete penetration detection, contact boundary smoothness and finite element discretization are an open problem in finite element analysis. To overcome this challenge, a stabilization scheme for small deformations [45], a continuous penalty force approach [40], contact based remeshing, and smoothing contact boundaries through Bezier patch approximations [35] have been proposed. Unfortunately, these approaches severely impact the computational performance especially as our insertion simulations are run for each shape hypothesis of  $\mathcal{A}$  being optimized. We thus limit our improvements to edge/face refinements, which only reduce contact force oscillations through a better approximation of continuous contact. However, arbitrary shapes with non-smooth boundaries and finite element discretization still produce non-smooth force profiles (Figure 6).

*Boundary and Initial Conditions.* During contact simulations,  $\mathcal{O}$  is constrained to move along a prescribed insertion path (*e.g.*, horizontally left in (Figure 7)).  $\mathcal{A}$  is displacement-constrained only along the insertion axis while leaving the remaining two orthogonal axes unconstrained (vertical and out of page). This allows non-symmetrical rigid objects or compliant structures to be

coupled in ways that minimize the total elastic energy without introducing artificial barriers to natural accommodative movements. As shown in Figure 7, this enables a more realistic identification of the true stress state of  $\mathcal{A}$ .

Users may define custom insertion paths for  $\mathcal{O}$  involving both translations and rotations when desired. However, unless specified otherwise, we assume the objects are inserted purely translationally without any rotations.

Due to the non-linear nature of (1), seeding it with a suitable initial condition is crucial for achieving robustness. We use the deformed state of the previous step as the initial condition for the current step.

## 5. Rest Shape Optimization

The insertion simulation allows its results to inform shape optimization on  $\mathcal{A}$  to produce a desired coupling behavior.

### 5.1. Shape Modification

To alter  $X$ , the rest shape of  $\mathcal{A}$ , we use linear blend skinning (LBS) with bounded bi-harmonic weights [46]. Using bounded bi-harmonic weights, we achieve smooth modifications in a localized and shape-aware manner. We use translation and scaling edits to facilitate a fine control over the structural dimensions of  $\mathcal{A}$ . For a mesh  $\mathcal{M}$  with  $n$  vertices in  $\mathbb{R}^d$  ( $d = 2$  or  $3$ ) and  $m$  modification handles

$$X' = M_{LBS}T, \quad (5)$$

where  $X' \in \mathbb{R}^{n \times d}$  is the matrix with the modified vertex positions in the rows,  $M_{LBS} \in \mathbb{R}^{n \times ((d+1)m)}$  is the linear blending skinning matrix computed once for the original mesh  $\mathcal{M}$ , and  $T \in \mathbb{R}^{((d+1)m) \times d}$  is a stack of handle transformation matrices that includes translations and scaling for each handle. For brevity, we refer to the translation and scale of the transformation handles as  $h$ .

The LBS formulation can be equivalently expressed in the following form

$$\mathbf{x}' = \sum_j w_j(\mathbf{x}) T_j \mathbf{x} \quad (6)$$

where  $T_j$  represents the affine transformations of a modification handle  $h_j$ ,  $j = 1, \dots, m$ . When transposed  $T_j$  matrices are stacked together, they form matrix  $T$  in Eq. (5). All vertex positions,  $\mathbf{x}$ , of  $\mathcal{M}$  are modified as  $\mathbf{x}'$ .  $w_j$  is the weight functions associated with the handle  $h_j$  and we compute them using bounded bi-harmonic weights [46]. These weights sum up to 1 at each vertex. Each handle has the maximum effect around its immediate neighborhood ( $w_j = 1$  at the handle) and its influence disappears at distant regions.  $M_{LBS}$  matrix is computed combining vertex positions  $\mathbf{x}$  with vertex weights  $w_j(\mathbf{x})$ .

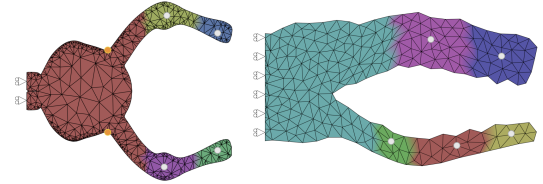


Figure 8: Handle placement through displacement based clustering. The left most edges of the objects are fixed as boundary conditions and we do not place handles on the corresponding clusters.

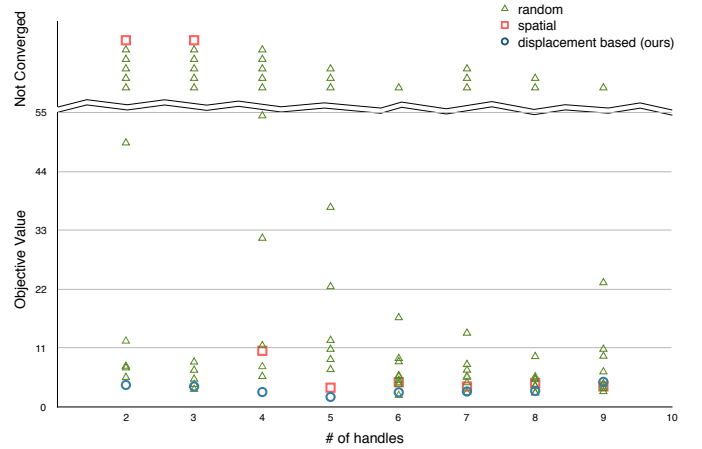


Figure 9: Displacement based, spatial, and random handle placements. Above the broken line, we report the handle placements that do not converge.

*Displacement Based Handle Placement.* To place the deformation handles  $h$  within  $\mathcal{A}$ , we perform an initial insertion simulation with the original  $\mathcal{A}$ . During the insertion process we record the maximum displacement each vertex undergoes. Then, we cluster the nodes of  $\mathcal{A}$  using  $\mathcal{M}$  as the connectivity graph, where the similarity between neighboring nodes is calculated based on their maximum displacements. In our implementation, we use the affinity propagation clustering method [47]. We take the vertex closest to the centroid of a cluster as the deformation handle for that cluster (Figure 8). We omit the clusters that include the displacement boundary conditions as they represent the clusters with minimal deformations. Nevertheless, we add displacement-constrained vertices as inactive handles to keep those regions unmodified during shape modifications. Note that this only affects shape updates, and not the nature of the boundary conditions during insertion simulations. Additional inactive handles (highlighted in orange) may be added to keep certain parts of the shape unchanged (refer to Section 6.1: Grip Control).

Figure 9 shows the impact of various choices for  $h$  for the same initial structure, objective function, and constraints (defined in Section 5.2). For each number of handles, we positioned them using our approach, using spatial clustering where vertex coordinates are used for similarity, and using 10-fold random pick of the handles. The results suggest that the handles do not have to be placed precisely. In particular, as the number of handles increases, up to

90% of the results expectedly converge even with random handle placement. However, our approach converges to a better solution that creates a minimal deviations in the shape. Spatial clustering also provides good handle placement and can be used if the initial insertion simulation cannot be performed.

## 5.2. Optimization

For the current shape hypothesis of  $\mathcal{A}$ , insertion simulations are performed producing the energy and force profiles. The relevant quantities are extracted from these profiles to compute the prescribed objective values. The deformation handles  $h$  are then used to deform  $\mathcal{A}$  in a way that improves the objective function. Figure 10 shows a scenario where the objective is to match the prescribed force profiles as close as possible by minimizing the squared error between the target and the resulting force profiles. As shown, the target profiles can be matched arbitrarily closely with an increased number of handles, essentially allowing our approach to design custom stiffness profiles for arbitrary objects.

To facilitate high-level end-user specification of coupling behavior, we formulate our objective function as minimizing the change in the rest shape of  $\mathcal{A}$  as measured by the *modification energy*, using  $h$  as the design variables, subject to the functional constraints of: (i) *coupling ratio*, (ii) *grip force*, (iii) *insertion and removal forces*, and (iv) *material failure*.

**Coupling Ratio.** For a pair of objects to remain stably coupled, the elastic energy profile must exhibit a peak  $E_d^{max}$ , before settling in a lower steady state energy  $E_d^{ss}$  (Figure 4). If the value of  $E_d^{ss}$  is too close to the value of  $E_d^{max}$ , small perturbations could cause the couple to disengage abruptly by causing  $\mathcal{A}$  to eject  $\mathcal{O}$ . We thus define a stable coupling ratio constraint as follows:

$$E_{CR} \equiv (E_d^{ss}/E_d^{max}) * 100 - \kappa_{cr} < 0, \quad (7)$$

where  $\kappa_{cr}$  is a percentile introduced to keep the inserted object inside the compliant structure.  $\kappa_{cr}$  can take on two different values: (I)  $\kappa_{cr} = 95\%$  if the user desires a non-zero grip, or (II)  $\kappa_{cr} = 10^{-3}\%$  if the user desires a loose couple. While the actual values are set empirically, the key here is to enable a binary decision between tight versus loose grips. If the former is elected,  $E_{CR}$  simply ensures that there is a stable configuration that allows a valid coupling. The precise strength of the grip is determined by the grip forces as described next. For energy profiles that do not initially attain a steady state value (Figure 4(b)), we use the maximum energy as the steady state. This way,  $E_{CR}$  will be violated for the current  $\mathcal{A}$ , hence penalized during optimization, thereby helping to impart shape changes in  $\mathcal{A}$  that lead to stable coupled steady states  $E_d^{ss}$ .

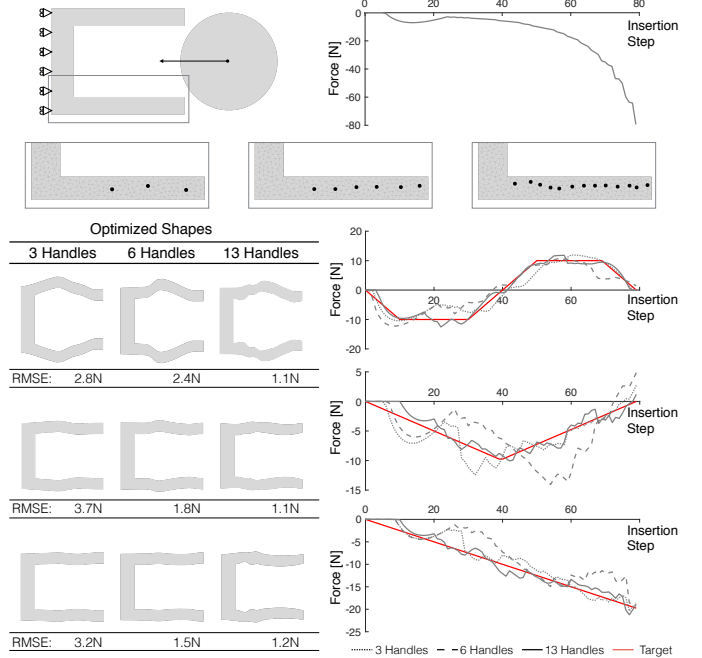


Figure 10: The compliant structure and its original force profile (top) is optimized to match prescribed force profiles. For different number of modification handles (middle), the target and the optimized force profiles are shown together with root-mean-square errors (bottom). Resulting force profiles show that our approach can alter the structure to match the target force profiles. This image is best viewed digitally.

**Grip Force.** Qualitatively, the grip force is a measure of how firmly  $\mathcal{A}$  squeezes  $\mathcal{O}$  when there are no other external forces and both parts are in static equilibrium. To quantify the grip, we decompose it into three components with the  $x$  component defined as:  $\mathbf{F}_g^x = 0.5 \sum_j |f_j^x| \quad \forall j \in \mathcal{M}$ , where  $f_j^x$  is the  $x$  component of the external force on vertex  $j$  imparted by  $\mathcal{O}$ . Note that only a subset of the boundary vertices of  $\mathcal{A}$  would contribute to  $\mathbf{F}_g^x$ .  $\mathbf{F}_g^y$  and  $\mathbf{F}_g^z$  are defined analogously. We finally define  $F_g$  to be the  $L_2$  norm of the resultant force vector  $[\mathbf{F}_g^x \mathbf{F}_g^y \mathbf{F}_g^z]$  and define the grip force constraint as:

$$\begin{aligned} E_{GT_1} &\equiv F_g^{lb} - F_g < 0, \\ E_{GT_2} &\equiv F_g - F_g^{ub} < 0, \end{aligned} \quad (8)$$

where  $F_g^{lb}, F_g^{ub}$  are the user specified lower/upper bounds on  $F_g$ .

**Insertion and Removal Forces.** We define the insertion and removal forces  $F_{in}, F_{rm}$  to be the maximum of the forces experienced by  $\mathcal{A}$  extracted from the deformation profiles (Figure 4) and constrain their values within user specified upper and lower bounds as follows:

$$\begin{aligned} E_{F_1} &\equiv F_{in} - F_{in}^{ub} < 0, \\ E_{F_2} &\equiv F_{in}^{lb} - F_{in} < 0, \\ E_{F_3} &\equiv F_{rm} - F_{rm}^{ub} < 0, \\ E_{F_4} &\equiv F_{rm}^{lb} - F_{rm} < 0, \end{aligned} \quad (9)$$

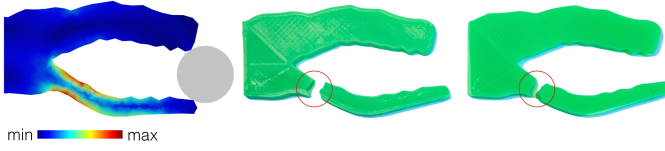


Figure 11: As our insertion simulations predict, the initial (unoptimized) shape breaks at the high stress region. Color plot shows the computed stresses (left). Two 3D prints of the initial design (middle, right) consistently break at the same location.

*Material Failure.* We consider yielding as the failure mode and use the von Mises stress criterion to constrain the stress developed in the compliant object during insertion. We enforce the yield criterion as a single constraint where we ask the maximum von Mises stress observed in the deformable object to be less than the yield stress.

$$E_{MF} \equiv \max(\sigma_{vm}) - \sigma_{yield} < 0 \quad (10)$$

*Modification Energy.* We use the Laplacian editing energy [48] of the surface mesh to quantify the total modification energy, also used by [15, 16].

$$\text{minimize } E_{\mathcal{L}} \equiv v_s^T M_{\mathcal{L}} v_s, \quad (11)$$

where  $M_{\mathcal{L}} = \mathcal{L}^T \mathcal{L}$  is a positive semidefinite matrix constructed using the surface Laplacian and calculated once for the original boundary mesh of  $\mathcal{A}$ .  $v_s$  denotes the modified boundary vertices.

The optimization seeks to minimize  $E_{\mathcal{L}}$  by modifying  $\mathcal{A}$  through the design vector  $h$ , while satisfying the constraints  $E_{CR}$ ,  $E_{GT}$ ,  $E_F$ , and  $E_{MF}$ . We transform this into an unconstrained problem by augmenting the objective,  $E_T$  with constraints as penalties. For any constraint  $c(h)$ , we transform it into a penalty  $c(h) \leftarrow \max(0, c(h))^2$  and add its contribution using a large penalty constant.

While we aim to establish a congruent scale for all constraint terms (percentages:0-100, stress:  $\sigma_{yield}$  around 60MPa for materials of interest, forces:1-100N range based on ergonomic limits [49]), this scheme would need adjustments if the scales of interest vary significantly.

We use simulated annealing for optimization and implemented it as described in [50]. A pseudo-code of our rest shape optimization is given in Algorithm 2. In each iteration of the optimization, we generate new states by sampling a new design vector around the current vector drawn from a Gaussian distribution, with an adaptive decaying variance. For cooling schedules, we experimented with linear, logarithmic, exponential cooling and observed similar convergence for our problem. In all of our examples, we are using exponential cooling.

## 6. Discussion & Results

We apply our shape optimization through deformation profiles on a variety of compliant structures with different

---

### Algorithm 2: Rest Shape Optimization

---

```

 $E_{curr} = E_{initial}, h_{curr} = h_{initial};$ 
 $E_{opt} = E_{initial}, h_{opt} = h_{initial};$ 
for  $i = 1$  to  $iterations_{max}$  do
     $h_i \leftarrow$  generate new neighbor state;
     $T_{curr} \leftarrow$  temperature cooling;
     $\mathcal{A}(h_i) \leftarrow$  update current shape hypothesis;
    perform an insertion simulation with  $\mathcal{A}(h_i)$ ;
     $E_d^{ss}, E_d^{max}, F_g, F_{in}, F_{rm} \leftarrow$  process deformation
    profiles;
     $E_i \leftarrow$  augment objective  $E_{\mathcal{L}}$  with penalty
    constraints  $E_{CR}, E_{GT}, E_F, E_{MF}$ ;
    if  $E_i < E_{curr}$  then
         $E_{curr} = E_i, h_{curr} = h_i;$ 
        if  $E_i < E_{opt}$  then
             $| E_{opt} = E_i, h_{opt} = h_i;$ 
        end
    else if  $\exp((E_{curr} - E_i)/T_{curr}) > \text{rand}(0, 1)$  then
         $| E_{curr} = E_i, h_{curr} = h_i;$ 
    end
end
return  $\mathcal{A}(h_{opt})$ 

```

---

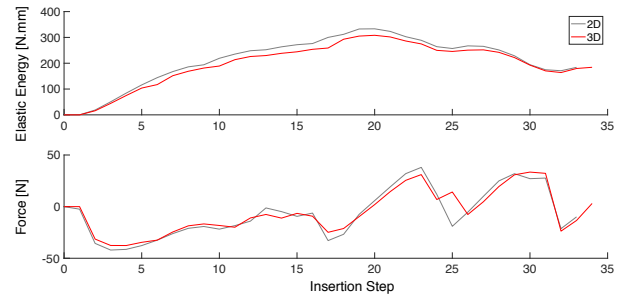


Figure 12: Comparison of insertion simulations for alligator model using 2D and 3D analysis. Plots are shown for the initial shapes.

behaviors. We present further details in the accompanying video.

### 6.1. Validation

*Insertion Simulations.* For the alligator presented in Figure 2, our simulations suggest that the initial unoptimized shape breaks during engagement with the stress distribution given in Figure 11. Printed physical samples break at the maximum stress region predicted by our simulations, supporting the boundary condition specifications (see the discussions of Figure 7). For this model, we also investigate the performance gain of a 2D analysis over a full 3D analysis. We obtain similar deformation profiles as shown in Figure 12. With 2D analysis, a considerable reduction in computation time is obtained due to the decrease in dimensionality as well as a reduction in the total number of vertices and elements. See Table 1 for a comparison of the computation time and the number of elements.

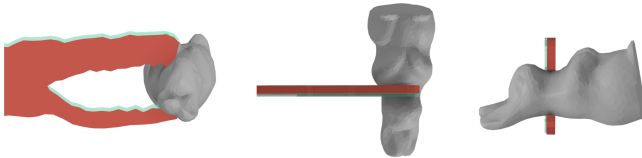


Figure 13: The shift in the alligator attachment during the insertion process from front, top and side views. The transparent green illustrates the original position.

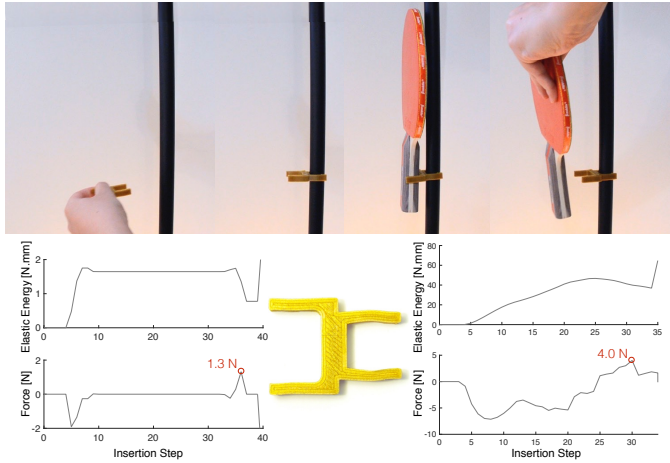


Figure 14: The paddle side is designed for a removal force less than the removal force on the stand side. The physical pull out of the paddle validates the design. Deformation profiles for both sides of the connector are also shown. Both sides have tight grips, but the paddle side requires a smaller removal force.

Figure 13 shows the bunny-in-alligator coupling. A vertical and out of page shift can be observed that correctly accommodates the tapered surface of the bunny.

*Force Control.* In Figure 14, we design a connector to attach a table tennis paddle to a cylindrical stand, with the paddle to be removed easily while the stand side remaining firmly attached. The resulting deformation profiles show this behavior with the stand side requiring a larger removal force.

*Grip Control.* We design a set of building blocks with fine-tuned physical grips as shown in Figure 15. Our approach decouples the grip force from the insertion and removal forces, thereby creating coupling behaviors that are not easily achievable through intuition alone. The deformation profiles capture the different grips as well as the tighter block interestingly requiring less insertion and removal forces (Figure 16). For this chain structure, to keep the rigid, inserted part identical in all designs, we add inactive handles (highlighted in orange in Figure 8) at the base of the arms so that the spherical body remains unchanged. We optimized the building blocks using a simplified 2D analysis and synthesized the 3D versions by revolving the base and replicating the optimized arms.

Figure 17 shows a door knocker that exhibits a loose grip. To simulate the coupling process, we use a rotating

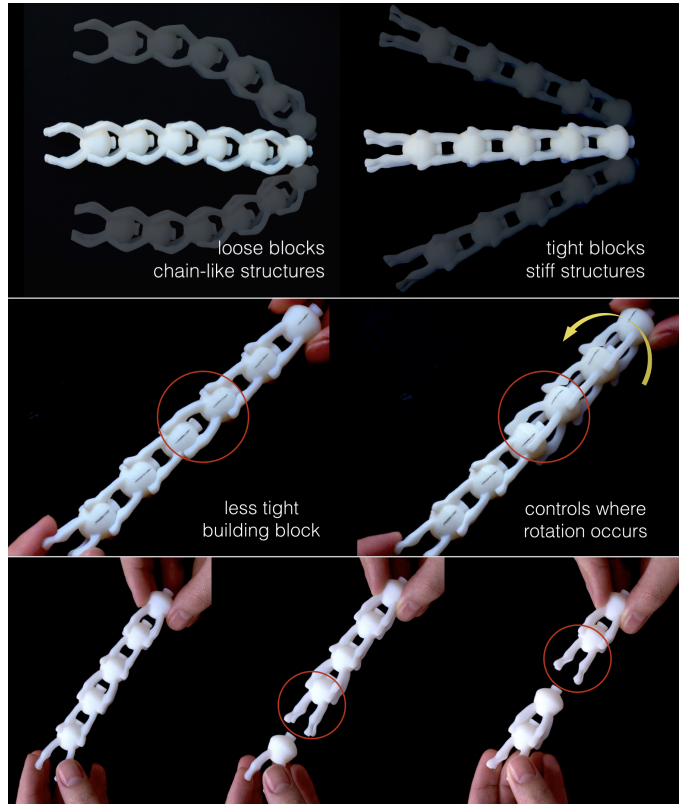


Figure 15: Starting from an initial geometry that barely stays together, we design building blocks with loose, tight and tighter grips. Using building blocks with different behaviors, we can build chain like structures, stiff structures (top) or combine them to control the motion transfer (middle). When we arrange the building blocks in an alternating order of tight and tighter grip ones, it separates from a block with tighter grip every time we pull from both ends (bottom). Notice tighter grips do not necessarily correspond to higher insertion/removal forces.

trajectory where the ring is initially inserted horizontally and rotated afterwards following the natural knocking motion. The initial shape not only requires excessive insertion forces on the order 4000 N, but it also readily yields with stresses up to 1425 MPa. When optimized, the insertion force is reduced down to 20 N, with a von Mises stress of 41 MPa (less than 60 MPa of yield stress).

Ergonomic grippers for handling common objects are popular items in 3D printing repositories. We demonstrate the design of an assistive door handle attachment with a tight grip for those with difficulty gripping door knobs in Figure 19. We also optimized the alligator to hold the bunny as shown in Figure 18. While the initial pairs cannot be coupled, the optimized alligator attaches to the bunny with a firm grip. In Figure 20, we optimize an initial mechanical claw that is unable to grab onto the bunny so that the resulting shape can latch onto it.

*Comparison.* In Figure 21, we compare our approach with AutoConnect [7] for two attachments. We optimize a connector that mounts the phone on its charger and a paddle attachment that connects the paddle to a cylindrical

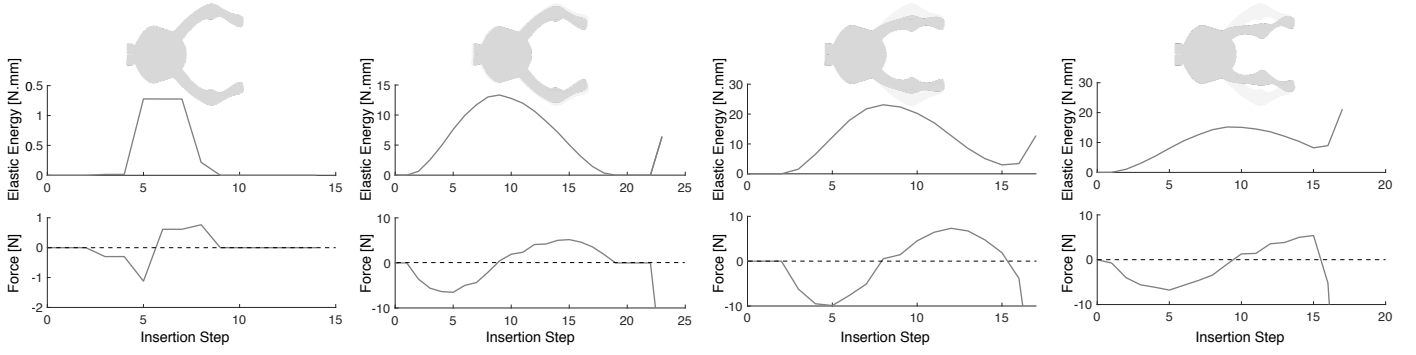


Figure 16: The initial shape is optimized through geometric changes to achieve loose, tight and tighter grip (from left to right). Deformation profiles are shown at the bottom with corresponding optimized shapes. Underlying silhouettes represent the initial geometries. Note that the loose design has zero steady state energy and the tight design has a non-zero steady state energy that is lower than the tighter design.

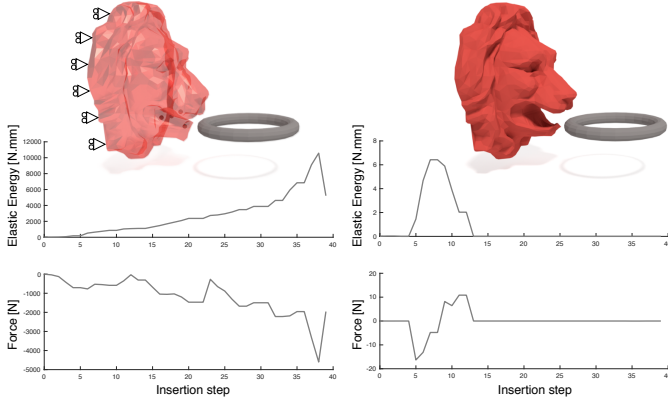


Figure 17: Initial system with boundary conditions and handles (left) and optimized (right) lion head model with their corresponding insertion simulations.



Figure 18: Initial alligator (a) is optimized (b) to hold the bunny (c). Printed and attached objects (d) exhibit the simulated/optimized behavior.

stand. For non-cylindrical and non-rectangular objects, Autoconnect generates rigid structures that the object is either slid in without deformations, or requires partitioned rigid attachments that are post-joined. Unlike AutoConnect, our method creates compliant structures for both the phone side and the paddle side of the connector. It modifies a starting geometry enabling easy insertion and removal, while producing a tight grip to hold the objects in place. For the stand side of the paddle attachment, our approach converges to a solution similar to AutoConnect’s standard C-clamp, while it begins with a square geometry. Similarly, we initialize the paddle side with a perfect match to the paddle’s cross section when attached (hence no deformation or grip) and converge to a firmly gripping structure.

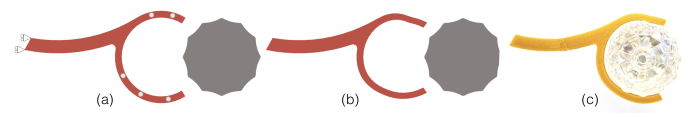


Figure 19: Assistive door handle (a) is optimized (b) to be attached on the door knob. The attachment (c) remains coupled while in use. Handles and boundary conditions are shown in (a).

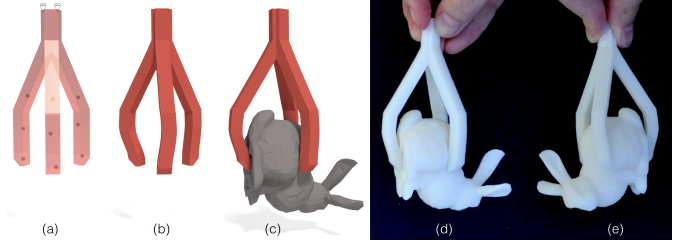


Figure 20: The initial mechanical claw (a) is optimized (b) to hold the bunny (c). Printed and attached optimized result is shown in (d) and (e). Handles and boundary conditions are shown in (a).

## 6.2. Physical Tests and Performance

*Fabrication.* We use a low cost FDM Printrbot as well as a Stratasys Objet Connex for fabrication, printing PLA and VeroWhite, respectively.

*Friction tests.* To study the impact of friction, we measured the insertion force of the same geometry with four different materials as 3D printed VeroWhite, acrylic, wood and metal using an Instron tensile testing machine (Figure 22). As expected, friction increases the required insertion force. Nonetheless, the physical measurements and our simulations exhibit similar trends in the profiles, differing primarily by a shift.

*Performance.* Shape updates and modification energy computations are expectedly fast. The insertion simulation is the computationally most demanding step in our approach. Table 1 shows the performance of our method using a 3.2GHz Intel Core i5 computer with 8GB memory. Because our rest shape optimization involves stochastic optimization, convergence speed may vary across different

Table 1: Statistics of the models used in our tests. For each model, we present # of simplex elements for attachment, # of vertices on the inserted object, # of modification handles, # of insertions steps, computation cost per iteration (one full insertion simulation).

Model	Elem.	Vert.	Handle	Insertion Steps	Time[s]
Stand Side	450	50	4	35	4.8
Paddle Side	1024	168	4	41	5.7
Building B.-L	896	142	4	25	4.5
Building B.-T1	896	142	4	25	4.5
Building B.-T2	896	142	4	25	4.5
Door Handle	1222	264	5	36	13.9
Alligator 2D	422	50	5	35	4.9
Alligator 3D	1040	1154	5	35	16.7
Alligator-Bunny	1040	1687	5	35	48.3
Door Knocker	5080	288	5	40	121.0
Charger Side	716	182	6	30	5.2
Phone Side	4110	20378	8	22	172.3
Claw	12063	11655	9	25	877.2

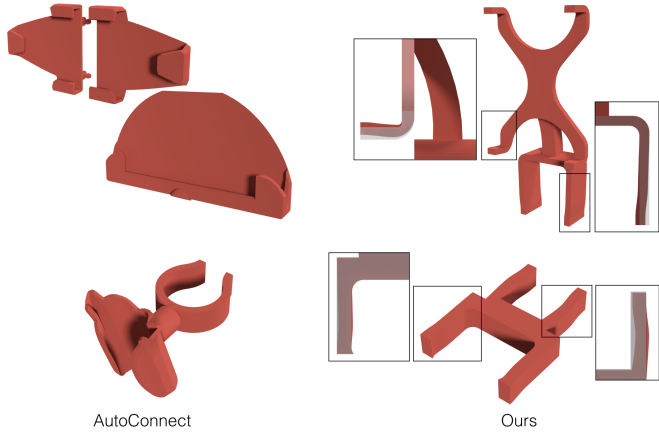


Figure 21: A comparison between AutoConnect [7] and our method. Our approach can create compliant attachments for phone (top) and paddle (bottom), while AutoConnect generates rigid holders when the objects are not cylinders or rectangular prisms.

runs of the same problem setting. For the results in this work, convergence is achieved under 300 iterations.

### 6.3. Limitations and Future Work

We do not remesh the compliant object during optimization; our estimations will likely become increasingly inaccurate due to degenerate elements if severe deviations from the original rest shape is required to achieve the desired coupling behavior. In this work, we meshed our initial geometries as uniform as possible to mitigate mesh dependency issues. We use Triangle [51] for 2D Delaunay meshing and TetGen [52] for tetrahedral meshing.

We do not model friction. Although friction based attachments are prone to wear and tear, there are use cases where a friction based attachment is required due to the object’s geometry and limiting surroundings. It is an interesting future direction to study friction-dominated coupling behaviors. Likewise, our method does not model the true surface contact area between the compliant structure and the inserted object. In some cases, increasing the contact area might be desirable to further increase grip

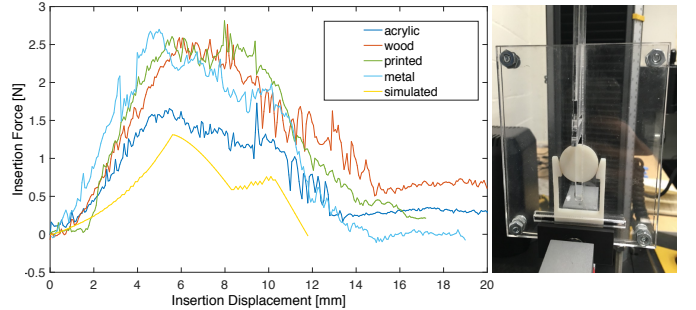


Figure 22: Effect of friction on insertion forces. The plots show insertion forces measured during the insertion of the same geometry manufactured with four different materials into one 3D printed attachment. Our simulations and the measurements exhibit similar profiles.

tightness. For example, our door handle and the knob contact each other at a limited set of discrete points whereas a larger contact area is likely more desirable to increase grip. However, this issue also highlights the difference between our definition of grip and that one experiences in real life. We quantify grip solely by the normal forces acting on the rigid object (squeeze force), while daily experience would also incorporate friction as part of this quantification (*e.g.*, how easy is it to rotate the objects relative to one another?).

Even though our algorithm reduces the stress and guarantees structural soundness during insertion, stress might still be concentrated around certain regions of the object which may limit fatigue performance. While we do not consider fatigue in this work, our work can be extended to account for this failure mode in the future.

While our method handles insertion paths that involve prescribed curved paths as well as prescribed rotations to the rigid object during engagement, a future extension would be to relax the rotary degrees of freedom during insertion. This would more closely mimic humans’ natural, accommodatory motions when coupling two objects.

## 7. Conclusion

Given a pair of arbitrary objects, we present a method to design targeted coupling behavior through shape modifications on the compliant object. Our approach does not rely on the knowledge of known contact points or deformed states. With our approach, non-intuitive coupling behaviors, such as firm grips requiring weak insertion/removal forces, can be designed. Our results demonstrate that free-form geometries can be geometrically altered to produce compliant attachments that expand the basic geometries of traditional attachments. This offers an opportunity for assistive design technologies where unique personal needs are present.

## 8. Acknowledgments

The authors would like to thank Kadri Bugra Ozutemiz, Robin Song and Nicholas Harrington for their help in physical testing.

## References

- [1] P. S. Stein, Mechanics of Materials, Pearson, 2012.
- [2] K.-J. Lu, S. Kota, Synthesis of shape morphing compliant mechanisms using a load path representation method, Vol. 5049, 2003, pp. 337–348. doi:10.1117/12.484020.  
URL <http://dx.doi.org/10.1117/12.484020>
- [3] K.-J. Lu, S. Kota, Topology and dimensional synthesis of compliant mechanisms using discrete optimization, *Journal of Mechanical Design* 128 (5) (2005) 1080–1091. doi:10.1115/1.2216729.
- [4] M. P. Bendsøe, Optimal shape design as a material distribution problem, *Structural optimization* 1 (4) (1989) 193–202.
- [5] J. Casals-Terre, A. Shkel, Dynamic analysis of a snap-action micromechanism, in: *Proceedings of IEEE Sensors*, 2004., 2004, pp. 1245–1248 vol.3. doi:10.1109/ICSENS.2004.1426406.
- [6] X. Chen, C. Zheng, W. Xu, K. Zhou, An asymptotic numerical method for inverse elastic shape design, *ACM Trans. Graph.* 33 (4) (2014) 95:1–95:11. doi:10.1145/2601097.2601189.  
URL <http://doi.acm.org/10.1145/2601097.2601189>
- [7] Y. Koyama, S. Sueda, E. Steinhardt, T. Igarashi, A. Shamir, W. Matusik, Autoconnect: Computational design of 3d-printable connectors, *ACM Trans. Graph.* 34 (6) (2015) 231:1–231:11. doi:10.1145/2816795.2818060.  
URL <http://doi.acm.org/10.1145/2816795.2818060>
- [8] B. Bickel, M. Bächer, M. A. Otraduy, H. R. Lee, H. Pfister, M. Gross, W. Matusik, Design and fabrication of materials with desired deformation behavior, *ACM Trans. Graph.* 29 (4) (2010) 63:1–63:10. doi:10.1145/1778765.1778800.  
URL <http://doi.acm.org/10.1145/1778765.1778800>
- [9] J. Panetta, Q. Zhou, L. Malomo, N. Pietroni, P. Cignoni, D. Zorin, Elastic textures for additive fabrication, *ACM Trans. Graph.* 34 (4) (2015) 135:1–135:12. doi:10.1145/2766937.  
URL <http://doi.acm.org/10.1145/2766937>
- [10] C. Schumacher, B. Bickel, J. Rys, S. Marschner, C. Daraio, M. Gross, Microstructures to control elasticity in 3d printing, *ACM Trans. Graph.* 34 (4) (2015) 136:1–136:13. doi:10.1145/2766926.  
URL <http://doi.acm.org/10.1145/2766926>
- [11] M. Skouras, B. Thomaszewski, S. Coros, B. Bickel, M. Gross, Computational design of actuated deformable characters, *ACM Trans. Graph.* 32 (4) (2013) 82:1–82:10. doi:10.1145/2461912.2461979.  
URL <http://doi.acm.org/10.1145/2461912.2461979>
- [12] J. Pérez, B. Thomaszewski, S. Coros, B. Bickel, J. A. Canabal, R. Sumner, M. A. Otraduy, Design and fabrication of flexible rod meshes, *ACM Trans. Graph.* 34 (4) (2015) 138:1–138:12. doi:10.1145/2766998.  
URL <http://doi.acm.org/10.1145/2766998>
- [13] H. Xu, F. Sin, Y. Zhu, J. Barbić, Nonlinear material design using principal stretches, *ACM Trans. Graph.* 34 (4) (2015) 75:1–75:11. doi:10.1145/2766917.  
URL <http://doi.acm.org/10.1145/2766917>
- [14] H. Xu, Y. Li, Y. Chen, J. Barbić, Interactive material design using model reduction, *ACM Trans. Graph.* 34 (2) (2015) 18:1–18:14. doi:10.1145/2699648.  
URL <http://doi.acm.org/10.1145/2699648>
- [15] R. Prévost, E. Whiting, S. Lefebvre, O. Sorkine-Hornung, Make it stand: Balancing shapes for 3d fabrication, *ACM Trans. Graph.* 32 (4) (2013) 81:1–81:10. doi:10.1145/2461912.2461957.  
URL <http://doi.acm.org/10.1145/2461912.2461957>
- [16] M. Bächer, E. Whiting, B. Bickel, O. Sorkine-Hornung, Spin-it: Optimizing moment of inertia for spinnable objects, *ACM Trans. Graph.* 33 (4) (2014) 96:1–96:10. doi:10.1145/2601097.2601157.  
URL <http://doi.acm.org/10.1145/2601097.2601157>
- [17] P. Musialski, T. Auzinger, M. Birsak, M. Wimmer, L. Kobbel, Reduced-order shape optimization using offset surfaces, *ACM Trans. Graph.* 34 (4) (2015) 102:1–102:9. doi:10.1145/2766955.  
URL <http://doi.acm.org/10.1145/2766955>
- [18] O. Stava, J. Vanek, B. Benes, N. Carr, R. Měch, Stress relief: Improving structural strength of 3d printable objects, *ACM Trans. Graph.* 31 (4) (2012) 48:1–48:11. doi:10.1145/2185520.2185544.  
URL <http://doi.acm.org/10.1145/2185520.2185544>
- [19] W. Wang, T. Y. Wang, Z. Yang, L. Liu, X. Tong, W. Tong, J. Deng, F. Chen, X. Liu, Cost-effective printing of 3d objects with skin-frame structures, *ACM Trans. Graph.* 32 (6) (2013) 177:1–177:10. doi:10.1145/2508363.2508382.  
URL <http://doi.acm.org/10.1145/2508363.2508382>
- [20] L. Lu, A. Sharf, H. Zhao, Y. Wei, Q. Fan, X. Chen, Y. Savoye, C. Tu, D. Cohen-Or, B. Chen, Build-to-last: Strength to weight 3d printed objects, *ACM Trans. Graph.* 33 (4) (2014) 97:1–97:10. doi:10.1145/2601097.2601168.  
URL <http://doi.acm.org/10.1145/2601097.2601168>
- [21] E. Ulu, J. McCann, L. B. Kara, Lightweight structure design under force location uncertainty, *ACM Transactions on Graphics (Proc. of SIGGRAPH 2017)* 36 (4).
- [22] G. Bharaj, D. I. W. Levin, J. Tompkin, Y. Fei, H. Pfister, W. Matusik, C. Zheng, Computational design of metallophone contact sounds, *ACM Trans. Graph.* 34 (6) (2015) 223:1–223:13. doi:10.1145/2816795.2818108.  
URL <http://doi.acm.org/10.1145/2816795.2818108>
- [23] N. Umetani, Y. Koyama, R. Schmidt, T. Igarashi, Pteromys: Interactive design and optimization of free-formed free-flight model airplanes, *ACM Trans. Graph.* 33 (4) (2014) 65:1–65:10. doi:10.1145/2601097.2601129.  
URL <http://doi.acm.org/10.1145/2601097.2601129>
- [24] N. Umetani, A. Panotopoulou, R. Schmidt, E. Whiting, Print-one: Interactive resonance simulation for free-form print-wind instrument design, *ACM Trans. Graph.* 35 (6) (2016) 184:1–184:14. doi:10.1145/2980179.2980250.  
URL <http://doi.acm.org/10.1145/2980179.2980250>
- [25] M. P. Bendsøe, O. Sigmund, Topology Optimization: Theory, Methods and Applications, Springer, 2004.
- [26] C. B. W. Pedersen, T. Buhl, O. Sigmund, Topology synthesis of large-displacement compliant mechanisms, *International Journal for Numerical Methods in Engineering* 50 (12) (2001) 2683–2705. doi:10.1002/nme.148.  
URL <http://dx.doi.org/10.1002/nme.148>
- [27] M. M. Shalaby, H. A. Hegazi, A. O. Nassee, S. M. Metwalli, Topology optimization of a compliant gripper using hybrid simulated annealing and direct search, in: ASME 2003 International Design Engineering Technical Conferences and Computers and Information in Engineering Conference, American Society of Mechanical Engineers, 2003, pp. 641–648.
- [28] D. Xu, G. Ananthasuresh, Freeform skeletal shape optimization of compliant mechanisms, *Journal of Mechanical Design* 125 (2) (2003) 253–261. doi:10.1115/1.1563634.
- [29] S. Nishiwaki, M. I. Frecker, S. Min, N. Kikuchi, Topology optimization of compliant mechanisms using the homogenization method, *International Journal for Numerical Methods in Engineering* 42 (3) (1998) 535–559.
- [30] T. E. Bruns, O. Sigmund, Toward the topology design of mechanisms that exhibit snap-through behavior, *Computer Methods in Applied Mechanics and Engineering* 193 (36 - 38) (2004) 3973 – 4000.
- [31] M. Ohsaki, S. Nishiwaki, Shape design of pin-jointed multistable compliant mechanisms using snapthrough behavior, *Structural and Multidisciplinary Optimization* 30 (4) (2005) 327–334. doi:10.1007/s00158-005-0532-2.  
URL <http://dx.doi.org/10.1007/s00158-005-0532-2>
- [32] M. Lawry, K. Maute, Level set shape and topology optimization of finite strain bilateral contact problems, arXiv preprint arXiv:1701.06092.

- [33] Y. Ling, Mating mechanics and stubbing of separable connectors, in: 1998 Proceedings. 48th Electronic Components and Technology Conference (Cat. No.98CH36206), 1998, pp. 6–13. doi:10.1109/ECTC.1998.678665.
- [34] Y.-L. H. Y.-L. Hsu, Y.-C. H. Y.-C. Hsu, M.-S. H. M.-S. Hsu, Y. Hsu, Shape optimal design of the contact springs of a connector, in: 2000 PCB Manufacturing Technology Conference, Yuan Ze University, Chung-Li, Taiwan, 2000.
- [35] G. Kloosterman, Contact methods in finite element simulations, Ph.D. thesis, University of Twente (2002).
- [36] W. A. McNeely, K. D. Puterbaugh, J. J. Troy, Six degree-of-freedom haptic rendering using voxel sampling, in: Proceedings of the 26th Annual Conference on Computer Graphics and Interactive Techniques, SIGGRAPH '99, ACM Press/Addison-Wesley Publishing Co., New York, NY, USA, 1999, pp. 401–408. doi:10.1145/311535.311600. URL <http://dx.doi.org/10.1145/311535.311600>
- [37] J. Barbić, D. L. James, Six-dof haptic rendering of contact between geometrically complex reduced deformable models, *IEEE Transactions on Haptics* 1 (1) (2008) 39–52. doi:10.1109/TOH.2008.1.
- [38] D. M. Kaufman, S. Sueda, D. L. James, D. K. Pai, Staggered projections for frictional contact in multibody systems, in: ACM SIGGRAPH Asia 2008 Papers, SIGGRAPH Asia '08, ACM, New York, NY, USA, 2008, pp. 164:1–164:11. doi:10.1145/1457515.1409117. URL <http://doi.acm.org/10.1145/1457515.1409117>
- [39] D. Harmon, E. Vouga, B. Smith, R. Tamstorf, E. Grinspun, Asynchronous contact mechanics, *ACM Trans. Graph.* 28 (3) (2009) 87:1–87:12. doi:10.1145/1531326.1531393. URL <http://doi.acm.org/10.1145/1531326.1531393>
- [40] M. Tang, D. Manocha, M. A. Otaduy, R. Tong, Continuous penalty forces, *ACM Trans. Graph.* 31 (4) (2012) 107:1–107:9. doi:10.1145/2185520.2185603. URL <http://doi.acm.org/10.1145/2185520.2185603>
- [41] E. Sifakis, J. Barbic, Fem simulation of 3d deformable solids: A practitioner's guide to theory, discretization and model reduction, in: ACM SIGGRAPH 2012 Courses, SIGGRAPH '12, ACM, New York, NY, USA, 2012, pp. 20:1–20:50. doi:10.1145/2343483.2343501. URL <http://doi.acm.org/10.1145/2343483.2343501>
- [42] R. Kolluri, Provably good moving least squares, in: Proceedings of the Sixteenth Annual ACM-SIAM Symposium on Discrete Algorithms, SODA '05, Society for Industrial and Applied Mathematics, Philadelphia, PA, USA, 2005, pp. 1008–1017. URL <http://dl.acm.org/citation.cfm?id=1070432.1070578>
- [43] J. Nocedal, S. J. Wright, Numerical Optimization, Second Edition, Springer, 2006.
- [44] M. ApS, The MOSEK optimization software (2015). URL <http://www.mosek.com> (2015)
- [45] P. Deuflhard, R. Krause, S. Ertel, A contact-stabilized newmark method for dynamical contact problems, *International Journal for Numerical Methods in Engineering* 73 (9) (2008) 1274–1290. doi:10.1002/nme.2119. URL <http://dx.doi.org/10.1002/nme.2119>
- [46] A. Jacobson, I. Baran, J. Popović, O. Sorkine, Bounded biharmonic weights for real-time deformation, in: ACM SIGGRAPH 2011 Papers, SIGGRAPH '11, ACM, New York, NY, USA, 2011, pp. 78:1–78:8. doi:10.1145/1964921.1964973. URL <http://doi.acm.org/10.1145/1964921.1964973>
- [47] B. J. Frey, D. Dueck, Clustering by passing messages between data points, *Science* 315 (5814) (2007) 972–976. doi:10.1126/science.1136800.
- [48] O. Sorkine, D. Cohen-Or, Y. Lipman, M. Alexa, C. Rössl, H. P. Seidel, Laplacian surface editing, in: Proceedings of the 2004 Eurographics/ACM SIGGRAPH Symposium on Geometry Processing, SGP '04, ACM, New York, NY, USA, 2004, pp. 175–184. doi:10.1145/1057432.1057456. URL <http://doi.acm.org/10.1145/1057432.1057456>
- [49] A. D. Astin, Finger force capability: measurement and prediction using anthropometric and myoelectric measures, Ph.D. thesis, Virginia Polytechnic Institute and State University (1999).
- [50] S. Kirkpatrick, C. D. Gelatt, M. P. Vecchi, Optimization by simulated annealing, *Science* 220 (4598) (1983) 671–680. doi:10.1126/science.220.4598.671. URL <http://science.sciencemag.org/content/220/4598/671>
- [51] J. R. Shewchuk, Triangle: Engineering a 2d quality mesh generator and delaunay triangulator, in: M. C. Lin, D. Manocha (Eds.), *Applied Computational Geometry Towards Geometric Engineering*, Springer Berlin Heidelberg, Berlin, Heidelberg, 1996, pp. 203–222.
- [52] H. Si, Tetgen, a delaunay-based quality tetrahedral mesh generator, *ACM Trans. Math. Softw.* 41 (2) (2015) 11:1–11:36. doi:10.1145/2629697. URL <http://doi.acm.org/10.1145/2629697>